Contrast transfer functions for Zernike phase contrast in full-field transmission hard X-ray microscopy

Yang Yang,[1,2,*] **Yin Cheng,**[1] **Ruth Heine,**[1] **and Tilo Baumbach**[1,3]

[1]*Institute for Photon Science and Synchrotron Radiation (IPS), Karlsruhe Institute of Technology (KIT), 76344 Eggenstein-Leopoldshafen, Germany*
[2]*Current address: European Synchrotron Radiation Facility (ESRF), 38043 Grenoble, France*
[3]*Laboratory for Applications of Synchrotron Radiation (LAS), Karlsruhe Institute of Technology (KIT), 76131 Karlsruhe, Germany*

[*]*yang.yang@esrf.eu*

Abstract: Full-field transmission hard X-ray microscopy (TXM) has been widely applied to study morphology and structures with high spatial precision and to dynamic processes. Zernike phase contrast (ZPC) in hard X-ray TXM is often utilized to get an in-line phase contrast enhancement for weak-absorbing materials with little contrast differences. Here, following forward image formation, we derive and simplify the contrast transfer functions (CTFs) of the Zernike phase imaging system in TXM based on a linear space-shift-invariant imaging mode under certain approximations. The CTFs in ZPC in their simplified forms show a high similarity to the one in free-space propagation X-ray imaging systems.

OCIS codes: (340.7460) X-ray microscopy; (340.7440) X-ray imaging; (110.4850) Optical transfer functions; (110.2990) Image formation theory.

References and links

1. W. Chao, B. D. Harteneck, J. A. Liddle, E. H. Anderson, and D. T. Attwood, "Soft X-ray microscopy at a spatial resolution better than 15 nm," Nature **435**, 1210–1213 (2005).
2. S.-C. Chao, Y.-C. Yen, Y.-F. Song, Y.-M. Chen, H.-C. Wu, and N.-L. Wu, "A study on the interior microstructures of working Sn particle electrode of Li-ion batteries by in situ X-ray transmission microscopy," Electrochem. Commun. **12**, 234–237 (2010).
3. C. A. Larabell and M. A. Le Gros, "X-ray tomography generates 3-D reconstructions of the yeast, Saccharomyces cerevisiae, at 60-nm resolution," Mol. Biol. Cell **15**, 957–962 (2004).
4. Y. Cheng, H. Suhonen, L. Helfen, J. Li, F. Xu, M. Grunze, P. A. Levkin, and T. Baumbach, "Direct three-dimensional imaging of polymer-water interfaces by nanoscale hard X-ray phase tomography," Soft Matter **10**, 2982–2990 (2014).
5. F. Xu, L. Helfen, H. Suhonen, D. Elgrabli, S. Bayat, P. Reischig, T. Baumbach, and P. Cloetens, "Correlative nanoscale 3D imaging of structure and composition in extended objects," PloS One **7**, e50124 (2012).
6. T. Bacquart, G. Devès, A. Carmona, R. Tucoulou, S. Bohic, and R. Ortega, "Subcellular speciation analysis of trace element oxidation states using synchrotron radiation micro-X-ray absorption near-edge structure," Anal. Chem. **79**, 7353–7359 (2007).
7. E. Nazaretski, K. Lauer, H. Yan, N. Bouet, J. Zhou, R. Conley, X. Huang, W. Xu, M. Lu, K. Gofron, S. Kalbfleisch, U. Wagner, C. Rau, and Y. S. Chu, "Pushing the limits: an instrument for hard X-ray imaging below 20 nm," J. Synchrotron Radiat. **22**, 336–341 (2015).
8. B. Bayerlein, P. Zaslansky, Y. Dauphin, A. Rack, P. Fratzl, and I. Zlotnikov, "Self-similar mesostructure evolution of the growing mollusc shell reminiscent of thermodynamically driven grain growth," Nat. Mater. **13**, 1102–1107 (2014).

#257148 Received 11 Jan 2016; revised 22 Feb 2016; accepted 23 Feb 2016; published 9 Mar 2016

9. H. Mimura, S. Handa, T. Kimura, H. Yumoto, D. Yamakawa, H. Yokoyama, S. Matsuyama, K. Inagaki, K. Yamamura, Y. Sano, K. Tamasaku, Y. Nishino, M. Yabashi, T. Ishikawa, and K. Yamauchi, "Breaking the 10 nm barrier in hard-X-ray focusing," Nat. Phys. **6**, 122–125 (2009).
10. J. Nelson, S. Misra, Y. Yang, A. Jackson, Y. Liu, H. Wang, H. Dai, J. C. Andrews, Y. Cui, and M. F. Toney, "In operando X-ray diffraction and transmission X-ray microscopy of lithium sulfur batteries," J. Am. Chem. Soc. **134**, 6337–6343 (2012).
11. T. dos Santos Rolo, A. Ershov, T. van de Kamp, and T. Baumbach, "In vivo X-ray cine-tomography for tracking morphological dynamics," Proc. Natl. Acad. Sci. USA **111**, 3921–3926 (2014).
12. A. Momose, "Recent advances in X-ray phase imaging," Jpn. J. Appl. Phys. **44**, 6355 (2005).
13. G. Schneider, "Cryo X-ray microscopy with high spatial resolution in amplitude and phase contrast," Ultramicroscopy **75**, 85–104 (1998).
14. D. B. Murphy and M. W. Davidson, *Fundamentals of Light Microscopy and Electronic Imaging* (Wiley-Blackwell, 2012).
15. Y. Liu, J. C. Andrews, J. Wang, F. Meirer, P. Zhu, Z. Wu, and P. Pianetta, "Phase retrieval using polychromatic illumination for transmission X-ray microscopy," Opt. Express **19**(2), 540 (2011).
16. Y. Yang, R. Heine, Y. Cheng, C.-C. Wang, Y.-F. Song, and T. Baumbach, "Approaching quantitative Zernike phase contrast in full-field transmission hard X-ray microscopy: Origin and reduction of artifacts," Appl. Phys. Lett. **105**, 094101 (2014).
17. H. Chen, Z. Wang, K. Gao, Q. Hou, D. Wang, and Z. Wu, "Quantitative phase retrieval in X-ray Zernike phase contrast microscopy," J. Synchrotron Radiat. **22**, 1056–1061 (2015).
18. I. Vartiainen, C. Holzner, I. Mohacsi, P. Karvinen, A. Diaz, G. Pigino, and C. David, "Artifact characterization and reduction in scanning X-ray Zernike phase contrast microscopy," Opt. Express **23**(10), 13278–13293 (2015).
19. S. Sugitani and K. Nagayama, "Complex observation in electron microscopy: III. inverse theory of observation-scheme dependent information transfer," J. Phys. Soc. Jpn. **71**, 744 (2002).
20. P. Cloetens, W. Ludwig, J. Baruchel, J.-P. Guigay, P. Pernot-Rejmánková, M. Salomé-Pateyron, M. Schlenker, J.-Y. Buffière, E. Maire, and G. Peix, "Hard x-ray phase imaging using simple propagation of a coherent synchrotron radiation beam," J. Phys. D Appl. Phys. **32**, A145 (1999).
21. P. Cloetens, M. Pateyron-Salomé, J. Buffiere, G. Peix, J. Baruchel, F. Peyrin, and M. Schlenker, "Observation of microstructure and damage in materials by phase sensitive radiography and tomography," J. Appl. Phys. **81**, 5878–5886 (1997).
22. P. Cloetens, R. Mache, M. Schlenker, and S. Lerbs-Mache, "Quantitative phase tomography of arabidopsis seeds reveals intercellular void network," Proc. Natl. Acad. Sci. USA **103**, 14626–14630 (2006).
23. K. A. Nugent, B. D. Arhatari, and A. G. Peele, "A coherence approach to phase-contrast microscopy: Theory," Ultramicroscopy **108**, 937–945 (2008).
24. B. Arhatari, A. Peele, K. Hannah, P. Kappen, K. Nugent, G. Williams, G. Yin, Y. Chen, J. Chen, and Y. Song, "A coherence approach to phase-contrast microscopy II: Experiment," Ultramicroscopy **109**, 280–286 (2009).
25. J. W. Goodman, *Introduction to Fourier Optics* (Roberts & Company, 2005).
26. K. Nagayama, "Another 60 years in electron microscopy: development of phase-plate electron microscopy and biological applications," J. Electron Microsc. **60**, S43–S62 (2011).
27. M. Howells, C. Jacobsen, T. Warwick, and A. Van den Bos, "Principles and applications of zone plate X-ray microscopes," in *Science of Microscopy*, (Springer, 2007), pp. 835–926.
28. J. P. Guigay, "Fourier transform analysis of fresnel diffraction patterns and in-line holograms," Optik **49**, 121–125 (1977).
29. J. P. Guigay, M. Langer, R. Boistel, and P. Cloetens, "Mixed transfer function and transport of intensity approach for phase retrieval in the fresnel region," Opt. Lett. **32**(12), 1617–1619 (2007).
30. J. Frank, *Three-Dimensional Electron Microscopy of Macromolecular Assemblies* (Academic, 1996).
31. J. Y. Huang, K. Jin, J. Lim, H. Kim, S. Jang, H. Choi, K. Gil, and S. Lee, "High-resolution and high-contrast bio-medical X-ray imaging by using synchrotron radiation in the PLS," J. Korean Phys. Soc. **56**, 2077 (2010).
32. M. Langer, P. Cloetens, and F. Peyrin, "Regularization of phase retrieval with phase-attenuation duality prior for 3-D holotomography," IEEE Trans. Image Process. **19**, 2428–2436 (2010).

1. Introduction

X-ray microscopy (XRM) in both *soft* and *hard* X-ray regimes has been utilized to probe with higher precision into small spatial and even temporal scales [1, 2] to access the morphology of macro- and micro- 3D structures [3, 4], as well as chemical information regarding elemental distribution and concentration [5], chemical states [6], etc.

Hard X-ray microscopy offers a non-invasive and versatile probe with varying spatial resolutions covering a wide range from a few hundred nm down to tens of nm [7, 8]. Bridging the gap between light microscopy and electron microscopy, it is becoming more and more crucial

#257148 Received 11 Jan 2016; revised 22 Feb 2016; accepted 23 Feb 2016; published 9 Mar 2016

in the mesoscopic regime in three dimensions [9]. Compared to soft XRM, hard XRM is more suited for investigations under more complex and flexible sample environments such as *in-situ* and *in-vivo* observation [10,11], probing non-invasively into three dimensions when combining with computed-tomography.

One of the major challenges for hard X-ray microscopy is related to the low sensitivity for distinguishing various structural components of light materials in biological specimens or composites of similar densities. Especially in life science, soft tissues or cells usually produce poor absorption contrast, i.e. small differences in image intensities that are merely observable. This is due to the fact that elemental compositions of low atomic numbers and low densities in soft tissues or cells are very similar to that of water [12]. Therefore in hard X-ray (>10 keV) regime, especially for light materials (low-Z elements) it becomes more interesting for imaging techniques to explore the phase shifts induced from the wave-matter interaction rather than modulations in amplitude. The sensitivity gain can reach up to an order of three magnitudes [12].

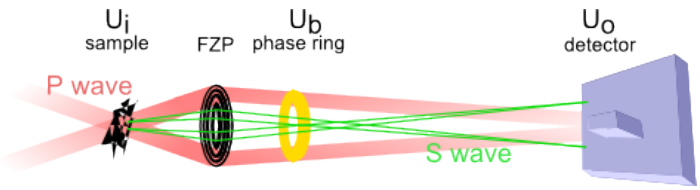

Fig. 1. Schematic layout of image formation in a TXM setup. The phase ring is placed in the back focal plane of the objective lens (Fresnel zone plate). U_i is the wavefield behind the sample. U_b is the wavefield behind the phase ring (in the back focal plane of FZP). U_o is the wavefield arriving at the detector plane. The P wave (red) represents the zeroth-order diffraction; the S wave (green) is the higher-order diffraction that passes the phase ring untouched. The interference between the phase altered P wave and the S wave will lead to contrast enhancement in the intensity recorded at the imaging plane.

Zernike phase contrast (ZPC) in full-field hard X-ray microscopy [13] integrates a phase ring in the back focal plane of the objective as shown in Fig. 1. By phase shifting the zeroth-order diffraction beam, namely, the primary beam, the recorded intensity of the interference between the primary wave and the diffracted wave can attain increased sensitivity particularly when applied to weak-absorbing objects. This enhanced contrast can be observed in-line and is approximately linearly proportional to the optical path difference (OPD), therefore implying the object-induced phase variation [14], which is the prominent advantage of ZPC.

However, due to its intrinsic low frequency artifacts from interference, to approach quantitative analysis remains difficult. Discussion began to emerge recently on how to tackle this problem. In general, one way to approach the quantification is off-line phase map retrieval using multiple radiographs under various conditions [15–17]. The other way is to modify the optics, such as the condensor and the coupled phase ring in order to suppress the ZPC artifacts [18].

Here, we would like to introduce and center on the contrast transfer functions (CTFs) of ZPC in full-field transmission hard X-ray microscopy in a simplified way under coherence assumptions. They have been derived as an extension of the formulation in electron microscopy [19], however they can be further simplified due to the properties of X-ray optics. Similarity can be found in CTFs of free-space propagation X-ray imaging system, which have been developed more than one decade ago [20] and have been extensively applied to make considerable achievements in varying research fields [21, 22]. Our derivation of simplified CTFs will be useful in deepening the understanding of this imaging system, with potential to improve the quantification of the image information.

#257148 Received 11 Jan 2016; revised 22 Feb 2016; accepted 23 Feb 2016; published 9 Mar 2016

2. Derivation of contrast transfer under Zernike phase contrast mode for full-field transmission X-ray microscopy

The TXM system can be modeled as a linear shift-invariant system composed of four parts, the input U_i, the lens, the Zernike phase ring U_b and the output U_o, as specified in Fig. 1.

A coherent illumination is assumed here while in practice it is generally taken as a mutually incoherent emission. Readers are referred to [23, 24] for the detailed discussion of coherence conditions. The complex transmission function of the sample can be linearized as follows

$$\begin{aligned} U_i(\mathbf{r}) = T(\mathbf{r})U_{source} &= \exp[-B(\mathbf{r}) + i\phi(\mathbf{r})] \\ &\approx 1 - B(\mathbf{r}) + i\phi(\mathbf{r}). \end{aligned} \tag{1}$$

Here $\mathbf{r}$ is the spatial coordinates in the transverse plane of the object, $\phi(\mathbf{r})$ is the relative phase variation in contrast to the amount of absolute phase shift $\Phi(\mathbf{r}) = \exp[(2\pi/\lambda)\int(1-\delta_n(\mathbf{r},z))\mathrm{d}z]$. δ_n is the real part of the complex refractive index of the medium. This linearization between the phase variation $\phi(\mathbf{r})$ and the transmission function of the object $T(\mathbf{r})$ is achieved by taking the assumptions of a weak-absorbing object with slowly varying phase shifts

$$B(\mathbf{r}) \ll 1, \quad |\phi(\mathbf{r}) - \phi(\mathbf{r}+\Delta\mathbf{r})| \ll 1. \tag{2}$$

The incident wavefield $U_i(\mathbf{r})$ is then forward propagated to the exit plane of the phase ring, which is also the back focal plane of the objective lens, where it equals [25]

$$U_b(\mathbf{f}) = \mathscr{F}\{U_i(\mathbf{r})\}A_p(\mathbf{f})H(\mathbf{f}). \tag{3}$$

$\mathbf{f}$ is the spatial frequency in Fourier domain corresponding to $\mathbf{r}$.

$$A_p(\mathbf{f}) = \begin{cases} \exp(i\theta_p)P(m,\lambda) = \exp(i\frac{3\pi}{2})P(m,\lambda) \text{ or } \exp(i\frac{\pi}{2})P(m,\lambda) & \text{if } \mathbf{f} \le f_p \\ 1 & \text{if } \mathbf{f} > f_p \end{cases}$$

is the pupil function of the phase ring. The cut-off spatial frequency f_p is defined as $f_p = \frac{r_p}{d_f\lambda}$, where d_f is the focal length of the objective lens, and r_p corresponds to the radius of the hole in the phase ring. The frequency f_p should be infinitely close to zero, since phase modification should only be applied to the zeroth-order diffraction beam. $P(m,\lambda)$ is the attenuation factor of the phase ring, depending on the materials (m) and the X-ray wavelength (λ).

$H(\mathbf{f})$ is the function characterizing optical deformation induced by the objective lens, including the pupil function, optical aberrations, and defocusing by shifting the lens, expressed in the form of [26]

$$H(\mathbf{f}) = \exp[-i\pi\Delta z\lambda\mathbf{f}^2 + g(\mathbf{f})]. \tag{4}$$

Here Δz denotes the defocusing distance, and $g(\mathbf{f})$ is the lens aberration factor, attributed to the optical aberrations inherent in the objective lens. In XRM systems with ZPC, the objective lens is mostly realized by a Fresnel zone plate (FZP). The FZPs in hard X-ray systems tend to have lower aberrations compared to lenses in electron microscopy or for soft X-rays because of their lower numerical apertures. Hence under the current diffraction resolution limit for hard X-rays [27], the spherical aberration as well as other aberrations can be safely neglected. In general, the pupil function of the FZP acts as a low-pass filter, limiting the achievable spatial resolution. As we focus our discussion on the transfer of the low frequencies, which carry the overall image contrast, this effect is not taken into account. Hence this pupil function is also neglected for simplicity.

#257148 Received 11 Jan 2016; revised 22 Feb 2016; accepted 23 Feb 2016; published 9 Mar 2016

By substituting Eq. (1) into Eq. (3), we get

$$\begin{aligned} U_b(\mathbf{f}) &= \mathscr{F}\{[1-B(\mathbf{r})]+i\phi(\mathbf{r})\}A_p(\mathbf{f})H(\mathbf{f}) \\ &= \{\exp(i\theta_p)P(m,\lambda)\delta(\mathbf{f})-\tilde{B}(\mathbf{f})+i\tilde{\phi}(\mathbf{f})\}H(\mathbf{f}) \\ &= \mathscr{F}\{U_i'(\mathbf{r})\}H(\mathbf{f}), \end{aligned} \tag{5}$$

from which we can observe that the ring functions as a high-pass phase shifter here since it in principle only modulates the phase of the Dirac delta function $\delta(\mathbf{f})$. In the end $U_i'(\mathbf{r})$ is the wavefield modified by the phase plate. Here $\tilde{B}(\mathbf{f})$ and $\tilde{\phi}(\mathbf{f})$ means $B(\mathbf{r})$ and $\phi(\mathbf{r})$ in Fourier space.

The image intensity in Fourier space at the imaging plane after far-field propagation can be written as an autocorrelation of the real space wavefield $U_i'(\mathbf{r})$ in the exit-plane of the objective lens [28]

$$\begin{aligned} \mathscr{F}\{I_o(\mathbf{f})\} &= |\mathscr{F}\{U_o(\mathbf{r})\}|^2 \\ &= \int U_i'(\mathbf{r}-\frac{\lambda\Delta z\mathbf{f}}{2})U_i'^*(\mathbf{r}+\frac{\lambda\Delta z\mathbf{f}}{2})\exp(-i2\pi\mathbf{f}\mathbf{r})\,\mathrm{d}\mathbf{r} \end{aligned} \tag{6}$$

in which $()^*$ means conjugation.

If we consider the wavefield $U_i'(\mathbf{r})$ in Fourier domain $\mathscr{F}\{U_i'(\mathbf{r})\} = \delta(\mathbf{f})-\tilde{B}(\mathbf{f})+i\tilde{\phi}(\mathbf{f})$ without the phase ring, i.e. in bright-field mode, and substitute Eq. (1) to Eq. (6) we get [29]

$$\tilde{I_o}(\mathbf{f}) = \delta(\mathbf{f})+2\sin(\pi\lambda\Delta z\mathbf{f}^2)\tilde{\phi}(\mathbf{f})-2\cos(\pi\lambda\Delta z\mathbf{f}^2)\tilde{B}(\mathbf{f}). \tag{7}$$

Here, the factor $\sin(\pi\lambda\Delta z\mathbf{f}^2)$ in front of the relative phase shifts $\tilde{\phi}(\mathbf{f})$ is defined as the phase contrast transfer function (phase CTF). And the factor $\cos(\pi\lambda\Delta z\mathbf{f}^2)$ in front of the absorption modulation $\tilde{B}(\mathbf{f})$ is the amplitude contrast transfer function (amplitude CTF).

Eq. (7) indicates a linear relation between the Fourier transform of the image intensity $\tilde{I_o'}(\mathbf{f})$ and the Fourier transform of the phase-amplitude modulation $\tilde{\phi}(\mathbf{f})$ and $\tilde{B}(\mathbf{f})$, with a small defocus distance Δz. This turns out to be one of the most important formulas in electron microscopy optics, and has been adopted to X-ray fields in the last decade [20,30]. The phase and amplitude CTFs in the equation each describe a spectral filter of the object information to pass through, and the resolution limit lies in the first zero crossings for a single record.

In Zernike phase contrast mode, for $U_i'(\mathbf{r})$ being phase modulated by θ_p and hence $\mathscr{F}\{U_i'(\mathbf{r})\} = \exp(i\theta_p)\delta(\mathbf{f})+\tilde{B}(\mathbf{f})-i\tilde{\phi}(\mathbf{f})$, the same amount of phase shift is induced in the transfer function and it becomes

$$\tilde{I_o'}(\mathbf{f}) = \delta(\mathbf{f})P^2+2\sin(\pi\lambda\Delta z\mathbf{f}^2+\theta_p)\tilde{\phi}(\mathbf{f})P-2\cos(\pi\lambda\Delta z\mathbf{f}^2+\theta_p)\tilde{B}(\mathbf{f})P. \tag{8}$$

When applying a $\theta_p = 3\pi/2$ phase ring, Eq. (8) can be reduced to

$$\tilde{I_o'}(\mathbf{f}) = \delta(\mathbf{f})P^2-2\cos(\pi\lambda\Delta z\mathbf{f}^2)\tilde{\phi}(\mathbf{f})P-2\sin(\pi\lambda\Delta z\mathbf{f}^2)\tilde{B}(\mathbf{f})P \tag{9}$$

which has the simplest form in the extreme case when $\Delta z = 0$, then $\tilde{I_o'}(\mathbf{f}) = \delta(\mathbf{f})P^2 - 2\tilde{\phi}(\mathbf{f})P$ [25], where the linearity between the phase modulation and the intensity can be achieved. Despite that this linearity can be inevitably corrupted by the inherent ZPC artifacts, the absorption contrast image can compliment to retrieve the phase map [16]. For concision, $P(m,\lambda)$ is noted as P in the equations.

One can also extend Eq. (8) to the dark field mode. Consider a beam stop with very high attenuation instead of the phase ring which blocks the direct beam, then we get

$$\tilde{I_o''}(\mathbf{f}) \approx 2\sin(\pi\lambda\Delta z\mathbf{f}^2+\theta_p)\tilde{\phi}(\mathbf{f})P-2\cos(\pi\lambda\Delta z\mathbf{f}^2+\theta_p)\tilde{B}(\mathbf{f})P \tag{10}$$

#257148 Received 11 Jan 2016; revised 22 Feb 2016; accepted 23 Feb 2016; published 9 Mar 2016

This imaging mode can be applied to observe e.g. scattering signals from ultra-structures [31].

It is obvious that the distinct difference of Eq. (9) from Eq. (7) is that the phase CTF is shifted from a sine function to a negative cosine function, while for the amplitude CTF an inverse change from a cosine to a sine function occurs.

This difference is a significant improvement in the final image intensity contrast in Zernike phase contrast mode, for the change of a sine function to a cosine function in phase contrast produces a much higher contrast factor for the low spatial frequencies, thus leading to much better preservation of the large features in the object. At the same time, a more smooth spectral distribution is obtained compared to the summed up defocusing CTFs [32], where multiple distances are often required in the regularization of the zero crossings in the summed CTFs.

Discussion on coherence condition and its influence in CTF

In experimental conditions, the illumination in TXM is usually assumed to be a quasimonochromatic Gaussian source distribution with a finite beam divergence and a finite energy spread. Regarding the aspect of temporal coherence corresponding to the energy spread, the transfer function will be the product of the coherent CTF with an envelope function characterizing the energy spread [30]. This damping effect in the CTFs will mainly contribute to the degrading of amplitude of CTFs and also to an elimination in the oscillations, leading to contrast depression and loss of fine details.

Concerning the spatial coherence, which can be characterized by the van Cittert-Zernike theorem with a complex coherence factor, its influence has been analyzed by K. A. Nugent in [23, 24]. In this study the impact of partial coherence on the contrast in microscopic systems is quantitatively analyzed. From the simulation, it is shown that under the same defocus distance the oscillations of both the amplitude and phase optical transfer functions (OTF) are rapidly suppressed as the coherence is reduced. It is more complicated than a simple envelope damping factor as in the temporal coherence case, but works in a similar manner in influencing the CTFs.

While the damping effect on CTFs may pose a trouble for defocusing algorithms which rely on a high degree of coherence, it will have less influence on Zernike phase contrast mode when phase retrieval is not required. Hence in this case the linearity of the exit wavefield does not need to be preserved, but it will become a linearity of the recorded image intensity instead [27].

3. Simulation of contrast transfer functions in TXM

To analyze the degree of contrast enhancement according to the CTF, the image of Lena is taken as the object for simulation. Image pixel size is set to be 30 nm, with image dimensions 20 µm by 20 µm. As a weak phase object with phase-attenuation duality, the phase shift ranges from 0.0029 to 0.039, and the amplitude attenuation is set to be even weaker by two orders of magnitude, what corresponds to typical values in biological applications. A small defocusing distance Δz of 150 µm is introduced here to both absorption and Zernike phase contrast modes. The amplitude and phase CTFs are first simulated independently of specific objects, and are only scaled by the defocusing distance Δz. So the further it is defocused, the narrower oscillations and zero crossings we get from the CTFs.

As shown in Fig. 2(a), in the bright-field (absorption) mode, the sine function of the phase CTF (green) stays below 0.5 for frequencies below below $2.7\,\mu\text{m}^{-1}$ (corresponding to 0.37 µm in real space). Hence it acts as a high-pass filter for the phase modulation factor $\tilde{\phi}(\mathbf{f})$, which is the dominating contrast in our object. This suppression of the low frequencies results in the poor visibility of the features larger than 0.37 µm. On the other hand, high frequencies are more prominent and manifested as sharply defined edges, corresponding to the edge-enhancement effect we obtained from defocusing propagation. This is the reason why weak absorbing objects usually can not be imaged truly but just the small variations and edges appear enhanced.

#257148 Received 11 Jan 2016; revised 22 Feb 2016; accepted 23 Feb 2016; published 9 Mar 2016

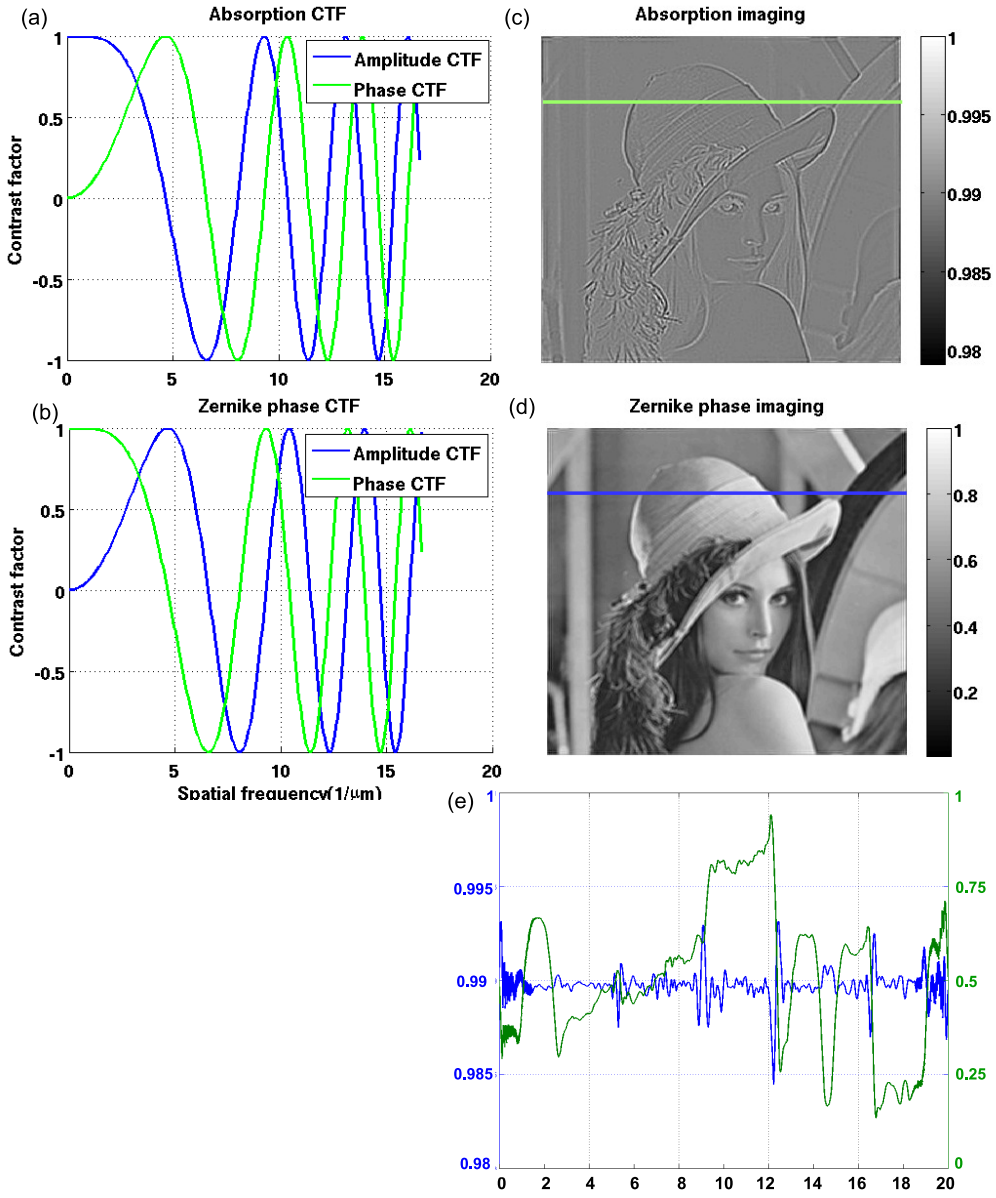

Fig. 2. Contrast transfer function (CTF) simulation and comparison between absorption mode and Zernike phase contrast mode in a TXM system. (a) Simulation of the amplitude and phase CTFs under absorption mode with a defocusing distance of 150 μm; (b) amplitude and phase CTFs under Zernike phase contrast mode with the same defocusing distance; (c) absorption image of the object, showing merely the edges of the object; (d) phase contrast image of the same object with the large scale features preserved; (e) comparison of line profiles of both (c) and (d).

In contrast, in Zernike phase contrast mode the phase CTF (green in Fig. 2(b)) is shifted by $3\pi/2$ to a cosine function, which is analogous to change a high-pass filter to a low-pass one. This change gives a boost to the final image contrast of the whole objects as the low

#257148 Received 11 Jan 2016; revised 22 Feb 2016; accepted 23 Feb 2016; published 9 Mar 2016

frequency information is much better preserved. The modulus of the phase CTF drops below 0.5 at the spatial frequency of $3.8\,\mu m^{-1}$ (which equals the fine features of $0.26\,\mu m$ in real space), indicating that fine features down to this threshold can be imaged. Compared to the absorption contrast Fig. 2(c), a clear improvement of visibility is obtained in the phase contrast image (d), which is also confirmed in the line profile comparison (e).

So for direct observation of weak absorbing objects, ZPC gains more sensitivity over absorption contrast. Furthermore, when the detection plane is close enough to the focus ($\pi\lambda\Delta z\mathbf{f}^2 \ll 1$), the phase CTF in Fig. 2(b) is stretched along the frequency axis, producing a more uniform spectral transfer of the phase information.

4. Summary

Based on a linear space-shift-invariant imaging model of a full-field transmission X-ray microscopy (TXM) system, the image formation and the contrast transfer functions (CTFs) of two contrast modes, absorption mode and Zernike phase contrast (ZPC) mode are presented. Under the assumptions of full coherence and weak-absorbing objects, we find a high similarity between the two CTFs. The main difference is the modulation factor multiplied to the object-induced phase shifts. Whereas it is a sine function for absorption contrast mode, it becomes a cosine function for ZPC mode because of the phase ring in the back focal plane of the zone plate. For objects with low-Z materials imaged with hard X-ray, considerable phase enhancement can be achieved since the cosine function, like a low-pass filter, will lead to better preservation of low frequencies and the overall image contrast improvement.

Benefiting from less optical aberrations in comparison to soft X-ray and electron microscopy, the CTF in TXM systems in the hard X-ray regime resembles the one in free-space propagation, which has been widely applied to quantitative phase retrieval. Hence this derivation of CTFs for a full-field microscopic system may be helpful for improvement on quantification of Zernike phase contrast imaging which is strongly desired in life science.

Appendix: derivation of contrast transfer function for Zernike phase contrast

From Eq. (6), by substituting Eq. (1) with a $3\pi/2$ phase modulation one can get

$$\begin{aligned}
\mathscr{F}\{I_o(\mathbf{f})\} &= \int U_i'(\mathbf{r}-\frac{\lambda\Delta z\mathbf{f}}{2})U_i'^{*}(\mathbf{r}+\frac{\lambda\Delta z\mathbf{f}}{2})\exp(-i2\pi\mathbf{f}\mathbf{r})\,\mathrm{d}\mathbf{r} \\
&= \int [-i-B(\mathbf{r}-\frac{\lambda\Delta z\mathbf{f}}{2})+i\phi(\mathbf{r}-\frac{\lambda\Delta z\mathbf{f}}{2})][-i-B(\mathbf{r}+\frac{\lambda\Delta z\mathbf{f}}{2})+i\phi(\mathbf{r}+\frac{\lambda\Delta z\mathbf{f}}{2})]^{*}\exp(-i2\pi\mathbf{f}\mathbf{r})\,\mathrm{d}\mathbf{r} \\
&= \int \{1+i[B(\mathbf{r}+\frac{\lambda\Delta z\mathbf{f}}{2})-B(\mathbf{r}-\frac{\lambda\Delta z\mathbf{f}}{2})]-[\phi(\mathbf{r}+\frac{\lambda\Delta z\mathbf{f}}{2})+\phi(\mathbf{r}-\frac{\lambda\Delta z\mathbf{f}}{2})]\}\exp(-i2\pi\mathbf{f}\mathbf{r})\,\mathrm{d}\mathbf{r} \\
&= \delta(\mathbf{f})+i\tilde{B}(\mathbf{r})[\exp(i\pi\lambda\Delta z\mathbf{f}^2)-\exp(-i\pi\lambda\Delta z\mathbf{f}^2)]-\tilde{\phi}(\mathbf{r})[\exp(i\pi\lambda\Delta z\mathbf{f}^2)+\exp(-i\pi\lambda\Delta z\mathbf{f}^2)] \\
&= \delta(\mathbf{f})-2\sin(\pi\lambda\Delta z\mathbf{f}^2)\tilde{B}(\mathbf{f})-2\cos(\pi\lambda\Delta z\mathbf{f}^2)\tilde{\phi}(\mathbf{f}) \qquad (11)
\end{aligned}$$

Acknowledgments

Y. Yang would like to thank Dr. Ralf Hofmann for the fruitful discussion. This research is under the support from Helmholtz-CSC scholarship. We acknowledge support by Deutsche Forschungsgemeinschaft and Open Access Publishing Fund of Karlsruhe Institute of Technology.

#257148 Received 11 Jan 2016; revised 22 Feb 2016; accepted 23 Feb 2016; published 9 Mar 2016